The interaction between atmospheric gravity waves and large-scale flows: an efficient description beyond the non-acceleration paradigm

Gergely Bölöni *

Institute for Atmosphere and Environment, Goethe University Frankfurt am Main, Germany.

Bruno Ribstein

Institute for Atmosphere and Environment, Goethe University Frankfurt am Main, Germany.

Jewgenija Muraschko

Institute for Atmosphere and Environment, Goethe University Frankfurt am Main, Germany.

Christine Sgoff

Institute for Atmosphere and Environment, Goethe University Frankfurt am Main, Germany.

Junhong Wei

Institute for Atmosphere and Environment, Goethe University Frankfurt am Main, Germany.

Ulrich Achatz

Institute for Atmosphere and Environment, Goethe University Frankfurt am Main, Germany.

**Corresponding author address:* Institute for Atmosphere and Environment, Goethe University Frankfurt am Main, Altenhöferallee 1, Frankfurt am Main, 60438, Germany.

E-mail: Boeloeni@rz.uni-frankfurt.de

ABSTRACT

With the aim of contributing to the improvement of subgrid-scale gravity wave (GW) parameterizations in numerical-weather-prediction and climate models, the comparative relevance in GW drag of direct GW-mean-flow interactions and turbulent wave breakdown are investigated. Of equal interest is how well Wentzel-Kramer-Brillouin (WKB) theory can capture direct wave-mean-flow interactions, that are excluded by applying the steady-state approximation. WKB is implemented in a very efficient Lagrangian ray-tracing approach that considers wave action density in phase-space, thereby avoiding numerical instabilities due to caustics. It is supplemented by a simple wave-breaking scheme based on a static-instability saturation criterion. Idealized test cases of horizontally homogeneous GW packets are considered where wave-resolving Large-Eddy Simulations (LES) provide the reference. In all of theses cases the WKB simulations including direct GW-mean-flow interactions reproduce the LES data, to a good accuracy, already without wave-breaking scheme. The latter provides a next-order correction that is useful for fully capturing the total-energy balance between wave and mean flow. Moreover, a steady-state WKB implementation, as used in present GW parameterizations, and where turbulence provides, by the non-interaction paradigm, the only possibility to affect the mean flow, is much less able to yield reliable results. The GW energy is damped too strongly and induces an oversimplified mean flow. This argues for WKB approaches to GW parameterization that take wave transience into account.

1. Introduction

The parametrization of gravity waves (GW) is of significant importance in atmospheric global circulation models (GCM), in global numerical weather prediction (NWP) models as well as in ocean models. In spite of the increasing available computational power and the corresponding increase of spatial resolution of GCMs and NWP models, for the time being, an important range of GW spatial scales remains unresolved both in climate simulations and in global NWP (Alexander et al. 2010). Numerous studies indicate that a representation of GWs is necessary for a realistic description of various aspects of the middle atmospheric circulation, e.g. the Brewer-Dobson circulation (Butchart 2014) and hence the zonal-mean winds and temperature (Lindzen 1981; Houghton 1978), the Quasi Biennial Oscillation (QBO) (Holton and Lindzen 1972; Dunkerton 1997), and Sudden Stratospheric Warmings (SSW) (Richter et al. 2010; Limpasuvana et al. 2012), and - via feedback loops - also the tropospheric circulation, e.g. the North Atlantic Oscillation (Scaife et al. 2005, 2012).

Parametrizations of the gravity wave drag are indeed applied in most GCMs or NWP models (Lindzen 1981; Medvedev and Klaassen 1995; Hines 1997a,b; Lott and Miller 1997; Alexander and Dunkerton 1999; Warner and McIntyre 2001; Lott and Guez 2013). Some way or other they all use Wentzel-Kramer-Brioullin (WKB) theory, however with some important simplifications, i.e. i) the assumption of a steady-state wave field and background flow, ii) the neglect of the impact of horizontal large-scale flow gradients on the GWs, and iii) one dimensional vertical propagation. Under these conditions the wave-dissipation or non-acceleration theorem states that GWs can deposit their momentum only where they break. In theoretical analyzes of this problem in a rotating atmosphere Bühler and McIntyre (1999, 2003, 2005) point out that the steady-state assumption can lead to the neglect of important aspects of the interaction between GWs and mean flow.

By wave-resolving numerical simulations and analyses on the basis of a nonlinear Schrödinger equation Dosser and Sutherland (2011) have demonstrated the relevance of direct GW-mean-flow interactions as well. Still missing, however, is an explicit assessment of the significance of the direct interaction between transient GWs and mean flow as represented by WKB - called *direct GW-mean-flow interactions* in the following. WKB modelling for diagnostic purposes, as by the GROGRAT model (Marks and Eckermann 1995, 1997), is a well-established tool (e.g. Eckermann and Preusse 1999), but such analyses leave out the GW impact on the large-scale flow. A semi-interactive approach to studies of the interaction between GWs and solar tides has been described by Ribstein et al. (2015), however with a simplified treatment of the GW impact on the solar tides, using effective Rayleigh-friction and thermal-relaxation coefficients. The numerical implementation of a *fully interactive* WKB theory, allowing direct GW-mean-flow interactions, is not a trivial task that should best be accompanied by validations against wave-resolving data. In a Boussinesq framework, the representation of direct GW-mean-flow interactions by a WKB algorithm has been been studied by Muraschko et al. (2015) for vertically propagating idealized wavepackets with variable vertical wavenumber. WKB theory had been implemented there in a 2-dimensional phase-space spanned by the physical height and the vertical wavenumber. The phase-space representation (Bühler and McIntyre 1999; Hertzog et al. 2002; Broutman et al. 2004) turned out to be effective to avoid numerical instabilities due to caustics, i.e. when ray volumes representing GWs become collocated in physical space but have different vertical wavenumbers and thus group velocities. Muraschko et al. (2015) could demonstrate the validity of their approach by comparisons against wave-resolving Large-Eddy-Simulation (LES) data.

The Boussinesq setting, however, leaves out the amplitude growth experienced by atmospheric GWs due to propagation into altitudes with decreasing density. That process, however, is central for the ensuing wave breaking due to static or dynamic instability at large GW amplitudes.

By the wave-dissipation theorem, steady-state GW parameterizations depend on wave breaking as the mechanism leading to a large-scale GW drag. How this mechanism - the only one represented by present GW parameterizations - competes with GW drag by direct GW-mean-flow interactions, and how well the latter can be captured in the atmosphere by a WKB algorithm have remained mainly unanswered questions to date. These are addressed here by investigations in a non-Boussinesq atmosphere, where the WKB algorithm is supplemented by a wave-breaking scheme. Steady-state WKB simulations are considered as well, representing the GW parameterization approach in present weather and climate models. As Muraschko et al. (2015) we consider idealized cases of upwardly propagating horizontally homogeneous GW packets. LES provide wave-resolving reference data.

Our investigations are described as follows: the theoretical background of the work is presented in section 2, while the corresponding numerical models are introduced in section 3. This is followed in section 4 by the presentation of the results. In section 5 the main findings of the work are summarized and conclusions are drawn.

2. Theoretical background

We are starting out from the compressible 2-dimensional Euler equations without rotation, which describe the evolution of the fluid in the $x-z$ plane:

$$\frac{Du}{Dt} + c_p\theta\frac{\partial\pi}{\partial x} = 0 \quad \text{with} \quad \frac{D}{Dt} = \frac{\partial}{\partial t} + u\frac{\partial}{\partial x} + w\frac{\partial}{\partial z} \tag{1}$$

$$\frac{Dw}{Dt} + c_p\theta\frac{\partial\pi}{\partial z} + g = 0 \tag{2}$$

$$\frac{D\theta}{Dt} = 0 \tag{3}$$

$$\frac{D\pi}{Dt} + \frac{\kappa}{1-\kappa}\pi\left(\frac{\partial u}{\partial x} + \frac{\partial w}{\partial z}\right) = 0 \tag{4}$$

where g is the gravitational constant, c_p denotes the heat capacity at constant pressure, R is the ideal gas constant, $\kappa = R/c_p$, $\pi = (p/p_0)^\kappa$ is the Exner pressure with p pressure and p_0 surface pressure, u and w are the velocity components in the $x-z$ plane. We assume that the flow consists of a reference part constant in time, a large scale background part and a small scale wave part both changing in time.

a. WKB theory

A notation for each variable in Eqs.(1)-(4) can be introduced as $f = \overline{f} + f_b + f_w$ where the first term denotes the reference part, with zero wind, while the other two refer to the large scale background and the wave parts, respectively. The flow is assumed to be periodic in x-direction. By linearization of Eqs.(1)-(4) about the reference and large scale background, introducing the wave pressure $p_w = (p_0/\kappa)\overline{\pi}^{\kappa-1}\pi_w$ and using an appropriate WKB scaling (see an explanation below), one obtains the Boussinesq polarization and dispersion relations at first order:

$$(U_w, W_w, B_w, P_w) = B_w \left(-i\frac{m}{k}\frac{\hat{\omega}}{N^2}, i\frac{\hat{\omega}}{N^2}, 1, -i\frac{m}{k^2}\frac{\hat{\omega}^2}{N^2} \right) \tag{5}$$

$$\hat{\omega} = \pm \frac{Nk}{\sqrt{k^2+m^2}} \tag{6}$$

where $\hat{\omega} = \omega - ku_b$ is the intrinsic frequency, and N denotes the Brunt-Väisälä frequency. In the polarization relation (5), U_w, W_w, B_w, P_w denote WKB wave amplitudes of u_w, w_w, b_w, p_w where $b_w = \frac{g}{\overline{\theta}}\theta_w$ is the wave buoyancy.

By appropriate WKB scaling it is meant that a scale separation between the potential temperature scale height and the wavelength is assumed, and that a corresponding WKB ansatz (Berethon 1966; Grimshaw 1975; Achatz et al. 2010; Rieper et al. 2013a) is imposed

$$f_w(x,z,t) = \Re F_w(z,t) e^{i[kx+\phi(z,t)]} \tag{7}$$

where k is a constant horizontal wavenumber, always assumed to be positive, the local phase ϕ defines the local vertical wavenumber $m = \partial\phi/\partial z$ and the local frequency $\omega = -\partial\phi/\partial t$. The wave amplitude F_w, the local frequency and vertical wavenumber, similarly to the large-scale background $f_b(z,t)$, are depending only slowly on z and t.

The WKB approximation at the next order leads to the wave action conservation equation

$$\frac{\partial \mathscr{A}}{\partial t} + \frac{\partial\left(c_{gz}\mathscr{A}\right)}{\partial z} = 0 \tag{8}$$

where $c_{gz} = \partial\omega/\partial m = \partial\hat{\omega}/\partial m$ is the vertical group velocity and $\mathscr{A} = E_w/\hat{\omega}$ is the wave action density with

$$E_w = \frac{\overline{\rho}}{4}\left(|U_w|^2 + |W_w|^2 + \frac{|B_w|^2}{N^2}\right) = \overline{\rho}\frac{|B_w|^2}{2N^2} \tag{9}$$

the wave energy. From the definition of the vertical wavenumber and frequency via the local phase, one derives a prognostic equation

$$\left(\frac{\partial}{\partial t} + c_{gz}\frac{\partial}{\partial z}\right)m = \mp\frac{k}{(k^2+m^2)^{1/2}}\frac{dN}{dz} - k\frac{\partial u_b}{\partial z} \equiv \dot{m} \tag{10}$$

for the vertical wavenumber. A solution method for the *field equations* (8) and (10) is the ray technique, observing that along characteristics, so-called ray trajectories, defined by $dz/dt = c_{gz}$, wavenumber and wave action density satisfy the *ray equations*

$$\frac{dz}{dt} = c_{gz} = \mp\frac{Nkm}{(k^2+m^2)^{3/2}} \tag{11}$$

$$\frac{dm}{dt} = \dot{m} \tag{12}$$

$$\frac{d\mathscr{A}}{dt} = -\frac{\partial c_{gz}}{\partial z}\mathscr{A} \tag{13}$$

where the dispersion relation (6) is used to calculate the local intrinsic frequency and hence the group velocity. By definition there is a unique wavenumber and a unique frequency at each vertical location.

The system is closed by a prognostic equation for the mean flow. Based on Achatz et al. (2010) and Rieper et al. (2013a), e.g., it is obtained as

$$\frac{\partial u_b}{\partial t} = -\frac{1}{\overline{\rho}}\frac{\partial}{\partial z}\left[\frac{\overline{\rho}}{2}\Re\left(U_w W_w^*\right)\right] \quad \text{with} \quad \frac{\overline{\rho}}{2}\Re\left(U_w W_w^*\right) = kc_{gz}\mathscr{A} \tag{14}$$

with * denoting the complex conjugate, and thus

$$\frac{\partial u_b}{\partial t} = -\frac{1}{\overline{\rho}}\frac{\partial}{\partial z}\left(kc_{gz}\mathscr{A}\right) \tag{15}$$

The problem with these equations (11) - (15) is that, after initialized from some fields of m, $\mathscr{A}$, and u_b, they very often lead to so-called caustics, where wavenumber, frequency, and wave-action density are not unique anymore. This happens when rays with different wavenumbers cross in space. Then the solution is not well defined anymore, and numerical instabilities become a serious problem (Rieper et al. 2013a) in attempts to obtain a local wavenumber by averaging the crossing rays. As demonstrated by Muraschko et al. (2015) in the Boussinesq context, however, this problem can be circumvented by considering the wave fields as a superposition of (infinitely) many WKB wave fields, characterized by a field index β, each having wavenumber and wave-action density m_β and $\mathscr{A}_\beta$ and satisfying equations (11) - (15) separately. In phase-space, spanned by wavenumber and position, here m and z, one introduces a wave-action density

$$\mathscr{N}(z,m,t) = \int_{\mathbb{R}} \mathscr{A}_\beta(z,t)\delta[m - m_\beta(z,t)]d\beta \tag{16}$$

with δ denoting the Dirac delta function. It can then be shown that

$$\frac{\partial \mathscr{N}}{\partial t} + \frac{\partial(c_{gz}\mathscr{N})}{\partial z} + \frac{\partial(\dot{m}\mathscr{N})}{\partial m} = 0 \tag{17}$$

and, since

$$\frac{\partial c_{gz}}{\partial z} + \frac{\partial \dot{m}}{\partial m} = 0 \tag{18}$$

also

$$\left(\frac{\partial}{\partial t} + c_{gz}\frac{\partial}{\partial z} + \dot{m}\frac{\partial}{\partial m}\right)\mathscr{N} = 0 \tag{19}$$

In this representation wavenumber is not a prognostic field, but a coordinate. The only wave field to be predicted is $\mathscr{N}$. Moreover, due to (18), the phase-space flow is volume preserving, so that rays cannot cross. Again one can resort to a ray technique, now however in phase-space. Defining the rays by their phase-space velocity $dz/dt = c_{gz}$ and $dm/dt = \dot{m}$, with $\dot{m}$ given by (10), one simply solves along these rays

$$\frac{d\mathscr{N}}{dt} = 0 \tag{20}$$

i.e. one keeps the conserved phase-space wave-action density along ray trajectories. For diagnostic purposes one can also determine the superposition of constituting wave-action densities

$$\mathscr{A}(z,t) = \int_{\mathbb{R}} \mathscr{A}_\beta(z,t)d\beta = \int_{-\infty}^{\infty} \mathscr{N}(z,m,t)dm \tag{21}$$

and the corresponding total wave energy density

$$E_w = \int_{-\infty}^{\infty} \hat{\omega}\mathscr{N}dm. \tag{22}$$

The ray equations are to be coupled to a mean flow equation with a wave impact that is the superposition of the wave impact of each of the constituting wave fields, characterized by m_β and $\mathscr{A}_\beta$, hence

$$\frac{\partial u_b}{\partial t} = -\frac{1}{\overline{\rho}}\frac{\partial}{\partial z}\left[\frac{\overline{\rho}}{2}\Re\int_{\mathbb{R}} d\beta\,\left(U_{w\beta}W_{w\beta}^*\right)\right] \quad \text{with} \quad \frac{\overline{\rho}}{2}\Re\int_{\mathbb{R}} d\beta\,\left(U_{w\beta}W_{w\beta}^*\right) = \int_{-\infty}^{\infty} kc_{gz}\mathscr{N}dm \tag{23}$$

and thus

$$\frac{\partial u_b}{\partial t} = -\frac{1}{\overline{\rho}}\frac{\partial}{\partial z}\int_{-\infty}^{\infty} kc_{gz}\mathscr{N}dm. \tag{24}$$

In a nutshell, the GW field and the mean flow are coupled and have an impact on the time evolution of each other: the GW field is influenced by the mean flow u_b via its impact on $\dot{m}$ and in turn the mean flow is modified by the GW phase-space wave-action density $\mathscr{N}$ via Eq.(24). This direct coupling is clearly transient. It is nonlinear, but different spectral components can only interact indirectly with each other, by GW-mean-flow interactions. Rigorously this is only correct at small amplitudes so that one might speak of a weakly nonlinear theory. As will be seen below, however, it yields quite useful results even at large amplitudes, close to breaking. Transience also means that wave propagation is described in a prognostic manner, different from present-day steady-state GW parameterizations where everything is instantaneous.

b. Wave breaking

As WKB theory does not account for the possible turbulent wave breakdown at large GW amplitudes, the coupled ray and mean flow equations above have been supplemented with a saturation criterion attempting the additional parametrization of this process. Comparisons between simulations with or without this ”turbulence scheme” also enable an assessment of the relevance of wave breaking for the GW drag, as compared to the direct GW-mean-flow interactions described by WKB.

It is assumed that saturation occurs if static-instability sets in at a certain height z during the wave propagation (Lindzen 1981) so that somewhere within a complete wave cycle $\partial \theta_w/\partial z + d\overline{\theta}/dz < 0$ or, after an additional multiplication by $g/\overline{\theta}$

$$\frac{\partial b_w}{\partial z} + N^2 < 0 \tag{25}$$

Comparison with (7) shows that this occurs in a locally monochromatic GW field if $|m||B_w| > N^2$ or, using Eq. (9),

$$2m^2 N^2 E_w/\overline{\rho} = m^2 |B_w|^2 > N^4 \tag{26}$$

We transfer this from the locally monochromatic situation to the spectral treatment represented by the phase-space approach by taking Eq.(22) into consideration, suggesting

$$\int_{-\infty}^{\infty} m^2 \frac{d|B_w|^2}{dm} dm = \frac{2N^2}{\overline{\rho}} \int_{-\infty}^{\infty} m^2 \hat{\omega} \mathcal{N} \, dm > \alpha^2 N^4 \tag{27}$$

The free parameter α represents well-known uncertainties of the criterion (25). Stability analyses (e.g. Lombard and Riley 1996; Achatz 2005) and direct numerical simulations (Fritts et al. 2003, 2006; Achatz 2007; Fritts et al. 2009) indicate that GWs are unstable already below the static-instability threshold, and strongly non-hydrostatic, modulationally unstable wavepackets also tend to break earlier (Dosser and Sutherland 2011). Another issue is that the criterion does not account for the possibility of destructive interference of different spectral components that would retard the onset of static-instability.

Once the static-instability criterion is satisfied at height z, turbulence is assumed to be generated that acts to damp wave-action density $\mathcal{N}$ to an extent that the GW field becomes again statically stable. Following Lindzen (1981) and Becker (2004), the turbulent fluxes are modeled by eddy viscosity and diffusivity so that small scales are damped more strongly than larger scales. The buoyancy equation, e.g., is supplemented by a a diffusion term

$$\frac{\partial b}{\partial t} = ... + K\left(\frac{\partial^2 b}{\partial x^2} + \frac{\partial^2 b}{\partial z^2}\right) \tag{28}$$

with the turbulent eddy diffusivity coefficient $K(z)$. By Fourier transformation in space and integration over a short time interval Δt one obtains as change of the buoyancy amplitude

$$\Delta\left|\tilde{b}\right|^2 = ... - 2K\Delta t\left|\tilde{b}\right|^2(k^2 + m^2) \tag{29}$$

Employing identical eddy viscosity and diffusivity an analogous equation

$$\Delta\left(\frac{d|B_w|^2}{dm}dm\right) = \frac{2N^2}{\overline{\rho}}\Delta\left(m^2\hat{\omega}\mathcal{N}dm\right) = -2K\Delta t\frac{2N^2}{\overline{\rho}}m^2(k^2+m^2)\hat{\omega}\mathcal{N}dm \tag{30}$$

can be derived for the wave amplitude. Hence after a saturation step

$$\frac{2N^2}{\overline{\rho}}\int_{-\infty}^{\infty} m^2\hat{\omega}\mathcal{N}[1 - 2K\Delta t(k^2+m^2)]dm = \alpha^2 N^4 \tag{31}$$

and thus the turbulent eddy diffusivity is computed as

$$K(z) = \frac{2\int_{-\infty}^{\infty} m^2\hat{\omega}\mathcal{N}dm - \alpha^2 N^2\overline{\rho}}{4\Delta t\int_{-\infty}^{\infty} m^2(k^2+m^2)\hat{\omega}\mathcal{N}dm}. \tag{32}$$

Further details regarding the numerical implementation of this wave-breaking parametrization are discussed in section 3c.

In summary, the weakly nonlinear coupled GW-mean-flow equations (11), (12), (20), and (24) describe the time evolution of a *transient* GW field through a *transient* large scale background flow in a *direct* manner. In addition wave breaking is accounted for in the WKB models by applying the saturation criterion (27) and reducing the wave action density proportionally to $K(z)$ as prescribed in (30), if necessary.

c. Steady-state WKB theory

As mentioned in the introduction, current GW parametrization schemes are based on a *steady-state* WKB theory (Nappo 2002; J.Coiffier 2011; Fritts and Alexander 2003; Kim et al. 2003). The assumption of a steady wave-action-density profile reduces (8) to

$$\frac{\partial}{\partial z}(c_{gz}\mathscr{A}) = 0 \tag{33}$$

Hence the pseudo-momentum flux $kc_{gz}\mathscr{A}$ is altitude-independent, and the GW drag in (15) vanishes. This is the non-acceleration paradigm. It is the reason why steady-state WKB schemes rely on wave breaking, thereby imposing a non-zero pseudo-momentum-flux convergence and hence tendencies for the induced wind. To compute the equilibrium profile of the wave field, first the vertical group velocity profile $c_{gz}(z)$ is obtained via (11) from a vertical wavenumber profile

$$m(z) = \sqrt{\frac{N^2(z)k^2}{(\omega - ku_b(z))^2} - k^2}, \tag{34}$$

where $\omega = ku_b(z = z_0) \pm N(z = z_0)k/(k^2 + m^2(z = z_0))$ is the constant extrinsic frequency, with z_0 a "source" altitude where vertical wave number and wave-action density are prescribed. From (33) one then obtains the wave-action-density profile

$$\mathscr{A}(z) = \frac{c_{gz}(z = z_0)\mathscr{A}(z = z_0)}{c_{gz}(z)}, \tag{35}$$

Wave breaking is assumed wherever the static-instability condition (26) is fulfilled, which amounts to setting the wave-action-density profile there to

$$\mathscr{A}(z) = \left| \frac{\alpha^2 N^2(z)\bar{\rho}(z)}{2m^2(z)\hat{\omega}(z)} \right|, \tag{36}$$

using the same α uncertainty parameter as explained in section 2b. Notably this approach leads to *instantaneous* pseudo-momentum-flux profiles. Variations of the boundary conditions at the source altitude are communicated immediately throughout the whole altitude range of a model, while in a more realistic transient approach any signal propagates at the group velocity. There are various possibilities of implementations of steady-state parameterizations (Fritts and Alexander 2003; Alexander et al. 2010), e.g. by allowing a spectrum via a superposition of components as just described, each with own values of vertical wave number and wave-action density at the source altitude. Lott and Guez (2013) e.g. suggest to pick these in a stochastic manner from a random sample. However, all of these approaches are instantaneous and they only allow GW-mean-flow interactions where GWs break.

3. Test cases and numerical models

Simulations have been done for a set of idealized test cases, where horizontally homogeneous quasi-monochromatic GW packets are initialized in an isothermal background with a reference temperature $T_0 = 300K$ resulting in a constant buoyancy frequency $N = \sqrt{g^2/c_pT_0} \approx 0.018\mathrm{s}^{-1}$. This implies a reference density profile

$$\overline{\rho}(z) = \rho_0 e^{-z/H_\rho} \quad \text{with} \quad H_\rho = RT_0/g \tag{37}$$

where H_ρ is the density scale height. Some of the test cases involve a prescribed background jet as an initial mean flow with a half-cosine wave shape

$$u_b(z) = \begin{cases} \frac{u_0}{2}\left[1+\cos\left(\frac{\pi(z-z_u)}{\Delta_u}\right)\right], & \text{if} \quad |z-z_u| \leq \Delta_u \\ 0, \quad \text{otherwise} \end{cases} \tag{38}$$

where u_0 is the maximal magnitude of the jet initialized at height z_u, and Δ_u is the width (i.e. vertical extent) of the half cosine shape. In these cases the wave-induced mean flow is diagnosed as $\hat{u}_b(z,t) = u_b(z,t) - u_b(z,t=0)$, i.e. the initial mean wind is subtracted from the total mean wind to get the one induced by the GW. We remark in this context that integrating (17) in wavenumber space, assuming a vanishing wave-action-density flux at the boundaries, and multiplying the result by the constant horizontal wavenumber yields, without saturation scheme,

$$\frac{\partial(k\mathscr{A})}{\partial t} = -\frac{\partial}{\partial z}\int_{-\infty}^{\infty} dm\, kc_{gz}\mathscr{N} \tag{39}$$

Therefore, comparing with (24), one obtains

$$u_b(z,t) = u_b(z,t=0) + \frac{1}{\bar{\rho}}\left[k\mathscr{A}(z,t) - k\mathscr{A}(z,t=0)\right] \tag{40}$$

so that $\hat{u}_b$ is in the absence of wave breaking the residual between $k\mathscr{A}/\bar{\rho}$, often termed the wave-induced wind, and its initial value.

The GW packets are initialized with a Gaussian or a cosine shaped buoyancy amplitude envelop in the vertical direction, i.e.

$$B_w(z) = a_0\frac{N^2}{m_0}\exp\left(-\frac{(z-z_0)^2}{2\sigma^2}\right), \quad \text{or} \quad B_w(z) = a_0\frac{N^2}{2m_0}\left[1+\cos\left(\frac{\pi(z-z_0)}{\sigma}\right)\right] \tag{41}$$

where z_0 is the height of the wave envelop maximum, m_0 is the initial vertical wavenumber and a_0 is the initial amplitude factor implying static-instability if $a_0 > 1$. The parameter σ defines the vertical size of the GW packet Δ_{wp}, namely $\Delta_{wp} \approx 5\sigma$ for the Gaussian wavepacket, while

$\Delta_{wp} = 2\sigma$ for the cosine shaped wavepacket. The envelop of the cosine-shaped wavepackets is limited to the interval $|z - z_0| \leq \Delta_{wp}$ i.e. $B_w(z) = 0$ outside this vertical range. In the horizontal x-direction, the wavepacket is initialized with infinite extent and a constant wavenumber k. In order to initialize the idealized wavepacket in the wave-resolving LES, the following perturbations are prescribed at initial time t_0:

$$b_w(x,z,t_0) = B_w(z)\cos(kx + m_0 z), \tag{42}$$

$$u_w(x,z,t_0) = B_w(z)\frac{m_0\hat{\omega}_0}{N^2 k}\sin(kx + m_0 z), \tag{43}$$

$$w_w(x,z,t_0) = -B_w(z)\frac{\hat{\omega}_0}{N^2}\sin(kx + m_0 z). \tag{44}$$

In the transient WKB simulations (we introduce this terminology for the non-steady-state WKB simulations) the GW packets are initialized via the corresponding monochromatic phase-space wave action density $\mathcal{N}$, i.e.

$$\mathcal{N}(z,m,t_0) = \frac{B_w^2(z)}{2N^2\hat{\omega}}\delta(m - m_0) \tag{45}$$

As a numerical representation of Eq. (45), the initial phase-space wave action density is set as:

$$\mathcal{N}(z,m,t_0) = \begin{cases} \dfrac{B_w^2(z)}{2N^2\hat{\omega}}\dfrac{1}{\Delta m_0}, & \text{if} \quad m_0 - \dfrac{\Delta m_0}{2} < m < m_0 + \dfrac{\Delta m_0}{2} \\ 0, & \text{otherwise} \end{cases} \tag{46}$$

where $\Delta m_0 = 10^{-4} m^{-1}$ is a narrow initial wavenumber width of the wavepacket. A typical value of the initial ratio in our numerical experiments is $\Delta m_0 / m_0 \approx 0.03$.

Seven idealized test cases have been investigated. Three cases elaborate the refraction and the reflection of hydrostatic GW packets from a background jet, while four other cases aim to study static and modulational instability of hydrostatic and non-hydrostatic wavepackets including the process of wave breaking. The initial wavepacket characteristics $z_0, k = 2\pi/\lambda_x, m_0 = 2\pi/\lambda_z, \Delta_{wp}$ and a_0 vary from case to case as well as the magnitude u_0 and height z_u of the jet. In all cases the negative frequency branch of Eq. (6) has been used so that positive vertical wavenumbers correspond to upwards directed group velocities. For the specific settings for each case see Tables 1 and 2 and the corresponding explanations in section 4. The LES resolution is $dx \approx \lambda_{x0}/30$, $dz \approx \lambda_{z0}/30$, while the WKB simulations have been done at a vertical resolution of $dz \approx \lambda_{z0}/10$, i.e. at a resolution three times coarser than the reference LES (see further details in Table 1 and 2). Both LES and WKB simulations with an increased resolution have been performed without observing significant changes in the results, which confirms that a convergence in the numerical results has been reached with the resolution described above.

a. Reference LES model

The reference LES model called *PincFloit* solves the pseudo-incompressible equations, i.e. a sound-proof approximation of the Euler equations (1)-(4) (Durran 1989). A third order Runge-Kutta time scheme and a finite volume spatial discretization is applied, which involves an Adaptive Local Deconvolution Model (ALDM) (Hickel et al. 2006) for turbulence parametrization. Alternatively, the MUSCL scheme, i.e. the Monotonic Upstream-Centered Scheme for Conservation Laws (van Leer 1979) can also be used in the finite volume scheme. Tests using both schemes for our cases did not show an important sensitivity. It is important to mention that in contrast to the WKB simulations the reference LES is fully nonlinear and enables the description of wave-wave interactions as well as turbulent wave dissipation, which, with a high resolution implies a realistic description of compressible flows. The *PincFloit* model has been described and tested in detail by Rieper et al. (2013b).

b. Eulerian WKB model

The Eulerian implementation of the WKB equations solves the flux form (17) of the phase-space wave-action density equation using the MUSCL finite volume discretization on the $z-m$ plane, with an equidistant staggered grid in both z- and m-direction. As a consequence the phase-space wave action density $\mathscr{N}$ and the derivatives $\partial u_b/\partial z$ and dN/dz are defined at cell-centers, while c_{gz} and $\dot{m}$ are defined at cell-edges as well as the rest of the variables including the wave energy E_w. In addition the mean flow equation (24) is solved using simple centered differences on the vertical part of the same staggered grid. A fourth order Runge-Kutta time scheme is used to evolve all the prognostic variables. A detailed description of the model, there in Boussinesq approximation, is given by Muraschko et al. (2015).

c. Lagrangian WKB model

The Lagrangian implementation of the WKB equations solves the advective form (19) of the phase-space wave-action density equation. This is done using a ray technique in phase-space. Defining the ray velocities by $dz/dt = c_{gz}$ and $dm/dt = \dot{m}$, with $\dot{m}$ given by (10), one simply solves (20) along these, i.e. one keeps the conserved phase-space wave-action density. This procedure is discretized numerically by gathering rays in finite ray volumes $\Delta m \Delta z$ around a characteristic carrier ray each, with uniform phase-space wave-action density $\mathscr{N}$ (see Fig. 1). By Eq. (20) that uniformity is conserved. Because the phase-space velocity is divergence free, each ray volume moreover preserves its volume content $a = \Delta m \Delta z$ in phase-space, but arbitrary shape deformations are possible. In a second discretization step we constrain each ray volume, however, to keep a rectangular shape, responding nonetheless, in a volume-preserving manner, to local stretching and squeezing. The prognostic equation for the evolution of the ray-volume edge length in m is given by

$$\frac{D_r}{Dt}(\Delta m) = \dot{m}(m_2, z) - \dot{m}(m_1, z) \tag{47}$$

with $m_1 = m - \Delta m/2$, $m_2 = m + \Delta m/2$ being the rectangle edges in m-direction. Due to the conserved area a the evolution Δz is given through Eq. (47) as well. The wave energy and the wave-induced mean wind are computed on an equidistant vertical grid, which is staggered in a consistent manner with the Eulerian WKB model regarding the background variables, the momentum flux and wave energy. The prediction of the mean flow is done as in the Eulerian model. Given that the distribution of the rays might get sparse in the vertical during the time evolution of the wave field, the projection of the momentum flux and the energy from the rays to the vertical grid is supplemented by a smoothing. This consists of computing the average over a certain number of neighboring vertical layers (the corresponding values are indicated for all numerical experiments in Tables 1 and 2). See Muraschko et al. (2015) for further specifications of the model. In comparison to that study, the reference density profile (37) has been implemented and used in the mean flow Eqs. (23)-(24). In line with this modification, the originally periodic bottom and upper boundary conditions have been changed to allow for a free outflow through these boundaries. This change was necessary given the realistic growth of wave amplitudes, which are due to the quasi-realistic density profile, and which are essentially non-periodic in vertical.

The wave-breaking parametrization has been implemented only in the Lagrangian model, since it is much more efficient than its Eulerian counterpart (see section 4a) and thus this is the WKB variant intended for future numerical studies. In the Lagrangian framework the analytical criterion (27) is to be rewritten as

$$\sum_{j=1}^{N_r^i} \left(m_j^i \left| {B_w}_j^i \right| \right)^2 \quad > \quad \alpha^2 {N^i}^4. \tag{48}$$

Here N_r^i is the number of ray volumes overlapping with layer i of the Lagrangian WKB model, with $i \in [1, nz]$ and with height $(i-1)dz < z(i) < idz$, nz being the number of vertical levels and $dz = L_z/(nz-1)$ the vertical resolution (layer depth) with L_z the height of the model top. m_j^i and $|B_{w_j}^{\ i}|^2$ are the wavenumber and squared wave buoyancy amplitude, respectively, of the carrier ray of the j-th ray volume relevant to layer i and N^i is the Brunt-Väisäalä frequency value at layer i. $\left(m_j^i \left|B_{w_j}^{\ i}\right|\right)^2$ is computed analytically from

$$\left(m_j^i \left|B_{w_j}^{\ i}\right|\right)^2 \quad = \quad \frac{2{N^i}^2}{\overline{\rho}^i}\left(\frac{\Delta z_i}{dz}\right)_j \int_{m_{j1}}^{m_{j2}} m^2 \hat{\omega} \mathcal{N} \, dm \tag{49}$$

where m_{j1} and m_{j2} are the edges of the j-th ray volume in m-direction so that $m_{j2} - m_{j1} = \Delta m_j$. The factor $\left(\frac{\Delta z_i}{dz}\right)_j$ denotes the fraction of the j-th ray being in the i-th vertical layer, as ray volumes might overlap with several vertical layers (see Fig.1). Using the dispersion relation (6) one obtains from Eq. (49)

$$\begin{aligned}
\left(m_j^i \left|B_{w_j}^{\ i}\right|\right)^2 &= \pm \frac{2{N^i}^3 k}{\overline{\rho}^i}\left(\frac{\Delta z_i}{dz}\right)_j \mathcal{N}_j \int_{m_{j1}}^{m_{j2}} \frac{m^2}{\sqrt{k^2+m^2}} dm \\
&= \pm \frac{2{N^i}^3 k}{\overline{\rho}^i}\left(\frac{\Delta z_i}{dz}\right)_j \mathcal{N}_j \frac{1}{2}\left[m_{j2}\sqrt{k^2+m_{j2}^2} - m_{j1}\sqrt{k^2+m_{j1}^2} \right. \\
&\quad \left. - k^2 \ln\left(\frac{m_{j2}+\sqrt{k^2+m_{j2}^2}}{m_{j1}+\sqrt{k^2+m_{j1}^2}}\right)\right]
\end{aligned} \tag{50}$$

If the saturation criterion is fulfilled in the i-th layer, the wave amplitude is reduced following (30) with Δt being the numerical time-step and K^i being the discretization of (32). The wave-action density after the saturation step then is

$$\mathcal{N}_j^{new} = \mathcal{N}_j \left[1 - 2K^i \Delta t \frac{\int_{m_{j1}}^{m_{j2}} m^2 (k^2+m^2)^{1/2} dm}{\int_{m_{j1}}^{m_{j2}} m^2 (k^2+m^2)^{-1/2} dm}\right] \tag{51}$$

d. Steady-state WKB model

A numerical model based on the steady-state WKB theory (section 2c) has been implemented as well, in order to enable a comparison with the transient WKB simulations and thus an assessment of present-day GW parameterizations. For optimal correspondence between transient and steady-state simulations, the time-dependent boundary values for wave number and wave-action density at the ”source” altitude z_0 in the steady-state simulation have been set to the corresponding values diagnosed from the transient simulation.

4. Results

We first give a comparative validation of the Eulerian and the Lagrangian WKB models, demonstrating the superiority of the latter. We then discuss a case where no wave breaking is active, but where the negligence of direct GW-mean-flow interactions would make a fundamental difference. Finally we compare the relative importance of direct GW-mean-flow interactions and of wave breaking in cases where both are active. There we also demonstrate the limitations of a steady-state approach with wave-breaking scheme.

a. Comparative validation of the Eulerian and Lagrangian WKB models

The refraction of a hydrostatic GW packet ($\lambda_{x0} = 10km, \lambda_{z0} = 1km$) by a jet has been studied using a conventional WKB ray-tracer in physical space by Rieper et al. (2013a). This WKB model failed to reproduce the LES simulation (see Fig.11a and Fig.11b in Rieper et al. (2013a)) and crashed due to numerical instabilities. These numerical instabilities were due to caustics, i.e. to rays crossing in physical space. A deliberate application of the phase-space representation to avoid numerical instabilities due to caustics was the main innovation of Muraschko et al. (2015), however in their study a Boussinesq reference atmosphere has been used, which did not allow an investigation of the case referred to in Rieper et al. (2013a). Thus, as a first proof of concept for the phase-space approach in an atmosphere-like configuration with a variable reference density, the very case described in Rieper et al. (2013a) has been revisited via LES and the transient phase-space WKB model simulations. A Gaussian-shape hydrostatic GW packet is initialized at an altitude of $10km$, propagating upwards and refracted by a low speed jet ($u_0 = 5ms^{-1}$) with its maximum at $25km$ (see case **REFR** in Table 1). The time evolution of the induced wind profiles is shown in Fig.2, which reveals a good correspondence between the transient WKB simulations and the LES (shaded colors). This proves that the phase-space approach applied in both WKB models helps avoiding numerical instabilities due to caustics and producing a realistic induced mean flow. Wave energy diagnostics of the transient WKB simulations compare to LES very well too (not shown).

If the jet blows in the appropriate direction ($u_b(z) > 0$ in case of the negative frequency branch), by increasing the speed of the jet, the refraction of the wavepacket turns into reflection due to the strong vertical wind shear and thus the intensive tendency in the vertical wavenumber (see Eq.(10)). A linear estimate for the jet speed threshold for reflection is (see e.g. the work of Muraschko et al. (2015))

$$u_{refl} = \frac{N}{k}\left(1 - \frac{k}{\sqrt{k^2 + m_0^2}}\right), \tag{52}$$

which in the current case gives $u_{refl} = 25.8ms^{-1}$. To achieve a reflection with full certainty and also to validate the models under strong-gradient conditions $u_0 = 40ms^{-1} > u_{refl}$ was chosen for our next case **REFL** (see details in Table 1). Note, that reflection also implies caustics, and thus could not be properly handled with a conventional ray.tracer. Also, reflection is a great challenge for the WKB theory in itself because it implies a change of sign of the wavenumber and thus an increase of the vertical wavelength far over the envelop scale, which breaks the scale separation assumption. In spite of these challenges the Lagrangian transient WKB simulation provides results with a good agreement with the LES, which is demonstrated in Figs. 3a and 3b by plotting the time evolution of the wave energy profile. It is apparent however in in Fig. 3c that the Eulerian transient WKB simulation does not produce a satisfactory reflection. This turned out to be due to the strong vertical wind shear, which made the Eulerian WKB code too diffusive, and thus almost fully dissipating the GW packet near the reflection level. By increasing the resolution of the Eulerian model by a factor of 10 in both z- and m-direction, a good agreement with the LES can be achieved (not shown), however at the same time the computational time gets exhaustive, i.e. $2-3$ times larger than the computing time of the LES! It is to be mentioned here, that even by using the same vertical resolution in the Eulerian and the Lagrangian transient WKB simulations, the latter is more efficient computationally than the former, by a factor of $10-100$ depending on the number of rays used in the Lagrangian model. The better efficiency of the Lagrangian model is due to the fact that in this framework i) there is no necessity to span the whole phase-space volume, including all its regions where the wave-action density is negligibly small, and ii) the prediction of the latter is done by solving the trivial conservation equation (20). In contrast, in the Eulerian model, the prognostic equation (17) is solved using the MUSCL finite volume scheme, which requires a relatively expensive reconstruction of the fluxes on the cell edges. These findings regarding the efficiency of the transient WKB simulations motivated the use of the Lagrangian model in all our further studies.

b. Role of direct GW-mean-flow coupling

Initializing a hydrostatic GW packet with somewhat shorter horizontal wavelength ($\lambda_{x0} = 6km$) and somewhat larger vertical wavelength ($\lambda_{z0} = 3km$) results in a reflection threshold $u_{refl} = 9.5ms^{-1}$ based on Eq.(52). An interesting experiment is to see whether the reflection happens if a jet speed maximum of $u_0 = 9.75ms^{-1} \approx u_{refl}$ is set (see case **PREFL** in Table 1). As shown in Fig.4a, the GW packet in the LES is only partially reflected and a part of the wavepacket is just refracted by the jet. This is due to the fact that Eq.(52) is a linear estimate for u_{refl} while the wave-mean-flow interaction is a nonlinear process as described by the LES. This shows that the linear approximation Eq.(52) is underestimating the jet speed threshold of reflection in a realistic nonlinear flow. The partial reflection, i.e. the behavior of the LES is qualitatively reproduced by the Lagrangian WKB model (Fig.4b), which suggests that the weakly nonlinear WKB dynamics are successful in capturing important aspects of the nonlinear interactions between the wave and the mean flow. What happens is that the GW packet based on Eq.(23) induces a wind, which is comparable to the jet speed but blowing in the opposite direction ($u_b < 0$) and thus reducing the net velocity of the jet. Indeed running the Lagrangian WKB model in a decoupled mode, i.e. ignoring Eq.(23) and thus not permitting the GW packet to modify the mean flow, the wavepacket is fully reflected as predicted by the linear estimate Eq.(52) (see Fig.4c). An additional experiment points out the importance of the variable reference density profile: the Lagrangian WKB model - in its coupled mode - predicts full reflection if a Boussinesq reference medium is used (Fig.4d). In this case, the weakly nonlinear wave-mean-flow interaction is active but, in the absence of amplitude growth due to the density effect, it is too weak to induce winds that are strong enough to alter the jet significantly. All this shows that during the propagation of GWs in an atmosphere-like medium from their source till their breaking levels, they continuously interact with their background flow and modify it significantly. In return to these wave-induced changes in the background flow the waves themselves can switch to inherently different regimes (e.g. changing the direction of propagation). No wave-breaking occurs in this case. Due to the non-acceleration paradigm, steady-state WKB simulations would therefore not be able to reproduce the observed dynamics.

c. Role of wave breaking

Finally, a set of cases with unstable GW packets or with GW packets turning into unstable regimes has also been studied. Comparisons between LES and transient WKB simulations with wave-breaking parameterizations serve to validate the latter. More important, however, these cases are to provide an assessment of the comparative importance of direct GW-mean-flow interactions, as represented by the WKB model without wave-breaking parameterization, and the wave breaking process itself, as represented by that latter turbulence scheme.

All of the cases are discussed in terms of the simple energetics that arises in WKB theory without rotation for horizontally homogeneous GW packets. Taking the time derivative of (22) and using the flux-form wave-action equation (17) one obtains

$$\frac{\partial E_w}{\partial t} = -\int dm \left[\frac{\partial(\hat{\omega} c_{gz}\mathcal{N})}{\partial z} + \frac{\partial(\hat{\omega}\dot{m}\mathcal{N})}{\partial m} - c_{gz}\dot{m}\mathcal{N} - \frac{\partial \hat{\omega}}{\partial N}\frac{dN}{dz} c_{gz}\mathcal{N}\right] \tag{53}$$

Inserting $\dot{m}$ from (10), and assuming a vanishing wave-action-density flux at the boundaries, yields

$$\frac{\partial E_w}{\partial t} = -\frac{\partial}{\partial z}\int dm\, c_{gz}\omega\mathcal{N} + u_b \frac{\partial}{\partial z}\int dm\, c_{gz}k\mathcal{N} \tag{54}$$

From (24), however, one finds that the time derivative of the mean flow kinetic-energy density

$$E_m = \frac{1}{2}\overline{\rho} u_b^2 \tag{55}$$

is

$$\frac{\partial E_m}{\partial t} = -u_b \frac{\partial}{\partial z}\int dm\, c_{gz}k\mathcal{N} \tag{56}$$

so that

$$\frac{\partial}{\partial t}(E_w + E_m) = -\frac{\partial}{\partial z}\int dm\, c_{gz}\omega\mathcal{N} \tag{57}$$

and hence the sum of wave energy and mean flow kinetic energy is conserved if the fluxes $\int dm\, c_{gz}\omega\mathcal{N}$ vanish at the vertical model boundaries. It thus makes sense to consider the vertically integrated energy densities

$$\bar{E}_w = \int_0^{L_z} dz\, E_w \tag{58}$$

$$\bar{E}_m = \int_0^{L_z} dz\, E_m \tag{59}$$

and their sum $\bar{E}_{tot} = \bar{E}_w + \bar{E}_m$. To do so we visualize normalized values

$$\hat{E}_m(t) = \frac{\bar{E}_m(t)}{\bar{E}_{tot}(t_0)} - \frac{\bar{E}_m(t_0)}{\bar{E}_{tot}(t_0)} \tag{60}$$

$$\hat{E}_w(t) = \frac{\bar{E}_w(t)}{\bar{E}_{tot}(t_0)} - \frac{\bar{E}_w(t_0)}{\bar{E}_{tot}(t_0)} \tag{61}$$

$$\hat{E}_{tot}(t) = \frac{\bar{E}_{tot}(t)}{\bar{E}_{tot}(t_0)} - 1 \tag{62}$$

In the first case a Gaussian-shape hydrostatic wavepacket ($\lambda_{x0} = 30km, \lambda_{z0} = 3km$) travels upwards and becomes statically unstable during the course of its evolution (see case **STIH** in Table 2). The results for this case are shown in Figs. 5a-d in terms of normalized integrated energy. The wave-breaking effect can be recognized in Fig. 5a at a decay of the total energy that is not visible in the results from the transient WKB simulation in Fig. 5b. Switching on the saturation scheme with $\alpha = 1$ (Fig. 5c), the GW energy, and hence also the total energy, gets reduced earlier than in the LES and also results in too weak an induced mean flow in the end. The total energy and the mean flow energy can be brought into better agreement with the LES by using the saturation scheme with $\alpha = 2$ (see Fig. 5d). The value $\alpha > 1$ suggests that the static-instability criterion as applied in this study is too strict, i.e. mimics wave breaking too early/strongly. This is presumably due to the neglect of the wave phase in the saturation scheme. Finally, by looking at Fig. 5a, it is apparent that except for the uppermost $10km$ in the induced wind, the transient WKB simulation reproduces the LES vertical structures already relatively well even without the wave saturation parametrization.

The evolution of a Gaussian-shape non-hydrostatic GW packet ($\lambda_{x0} = \lambda_{z0} = 1km$) is discussed next, which evolves quickly into a statically unstable regime, due to its high initial amplitude factor $a_0 = 0.9$ (case **STINH** in Table 2). The normalized energies of the LES in Fig.6a imply a decay of total energy that saturates by $t \approx 2N^{-1}$. This is not reproduced completely by the transient WKB simulation (Fig. 6b). By switching on the wave-breaking parameterization, however, with $\alpha = 1.4$

the LES results are met rather well (Fig.6c). As a reference the results on the energetics from the transient WKB simulation with saturation scheme and $\alpha = 1$ are also plotted in Fig. 6c (dashed curves). Again the dissipation is somewhat too strong, indicating that the static-instability criterion is too strict for best diagnosing saturation in the real atmosphere. The reduced optimal value of α compared to the previous case might be due to the added inclination of non-hydrostatic wavepackets to become modulationally unstable. By looking at the vertical structures of the wave energy and the induced mean wind in Figs. 6a-l one finds again that the wave-breaking parametrization provides only small corrections on top of the relatively good results provided by the transient WKB simulations without the saturation scheme.

The next case involves a cosine-shape non-hydrostatic GW packet ($\lambda_{x0} = \lambda_{z0} = 1km$), which becomes modulationally unstable during its evolution, i.e. its vertical wavelength grows beyond its horizontal wavelength so that $|m| < |k|/\sqrt{2}$ (see case **MI** in Table 2). In this regime the wave-induced mean flow accelerates the trailing edge and decelerates the leading edge of the wave envelop while the amplitude grows, leading to the collapse of the wavepacket due to local static-instability (Sutherland 2006, 2010; Dosser and Sutherland 2011). This same case has also been studied by Rieper et al. (2013a) where their conventional WKB code broke down due to numerical instabilities related to caustics, as explained in section 4a. In contrast to that study, the Lagrangian phase-space WKB model remains numerically stable and reproduces the LES results relatively well (Figs. 7a-i), with or without the wave-breaking parametrization. The integrated-energy plots in Figs. 7a-c suggest, however, that without the saturation scheme the induced mean flow is overestimated by the WKB model and a best fit to the LES is found if $\alpha = 0.6$ is used in the saturation scheme. The results with $\alpha = 1$ (Figs. 7c, dashed curves), however, are also quite acceptable.

Finally a hydrostatic GW packet ($\lambda_{x0} = 10km, \lambda_{z0} = 1km$) reaching a critical layer is studied. An easterly jet with a maximum of $u_0 = -11ms^{-1}$ is prescribed at $z_u = 25km$, so that without wave impact on the mean flow the intrinsic phase velocity would vanish at around $22-23km$ height (see case **CL** in Table 2). The transient WKB simulation without saturation scheme seems to slightly overestimate the mean flow energy compared to the LES, (Figs. 8a-b), which can be removed by switching on the saturation scheme with $\alpha = 1$ (Fig. 8c). This value of α suggests that in case of a critical layer, GWs tend to break as predicted by classic static-instability criteria.

Our results suggest that wave breaking is of secondary importance in comparison with the direct GW-mean-flow interactions even for large amplitude GWs. Since present-day GW-drag parameterizations exclusively rely on wave breaking the question arises what results they would yield in the cases considered. Therefore the cases **STIH**, **STINH**, and **MI** have been also been simulated using the steady-state WKB model based on sections 2c and 3d. Figure 9 shows the corresponding results for case **STINH**, which are to be compared with Fig.6, where the transient WKB and the LES results are shown. The integrated energy shows that the wave energy is over-damped and that the kinetic energy of the mean flow is strongly underestimated in the steady-state WKB model. The former is also observed in the Hovmöller diagram of the wave energy. The Hovmöller diagram of the induced mean wind shows that the magnitude of the GW drag is too small in the steady-state WKB model and also its structure is very different from that of the LES and the transient WKB simulation. One should of course restrict the comparison between the models to the vertical region above the source ($z_0 = 10km$), but there as well, the results from the steady-state WKB simulation show an unrealistic structure in the induced mean flow, seemingly fully determined by wave breaking. Again this demonstrates the dominant role of direct GW-mean-flow interactions as compared to wave breaking, and it also points to limitations of present-day GW parameterizations.

5. Summary and Conclusions

The steady-state approximation to WKB theory used nowadays in GW-drag parameterizations implies that the only GW forcing on the mean flow is due to wave breaking. Transient GW-mean-flow interactions can however act as another important coupling mechanism. This study provides an assessment of the comparative importance of these processes in typical atmospheric situations, albeit idealized. Focussing on single-column scenarios for the time being, considered GW packets are horizontally homogeneous and the mean flow has only a vertical spatial dependence. The wave scales and amplitudes, however, are representative, although not of inertia-gravity waves affected by rotation. Fully interactive transient WKB simulations are used to describe the simultaneous development of GWs and mean flow. All of these simulations are validated against wave-resolving LES, thereby assessing the reliability of the methods employed.

The WKB algorithms used allow the simulation of transient GW development. In both variants, Eulerian or Lagrangian, the mean flow is fully coupled to the wave field. This is enabled by a spectral approach, employing wave-action density in position-wavenumber phase-space, the key to avoiding otherwise detrimental numerical instabilities due to caustics. The Eulerian approach spans the whole phase-space. It thus quickly tends to be expensive, often more than LES. The Lagrangian ray-tracing approach, however, focusses on regions of phase-space with non-negligible wave action. This makes it considerably more efficient, by orders of magnitude, than the wave-resolving simulations. Certainly this might change in situations where broad spectra develop. So far, however, we have not met with such a case.

A systematic investigation of the comparative relevance of wave breaking, as compared to direct GW-mean-flow interactions, has been enabled by the implementation of a simple turbulence scheme. Turbulence is invoked whenever the wave field has the possibility to become statically unstable. A flux-gradient parameterization of turbulent fluxes is used, by way of eddy viscosity and diffusivity. The ensuing damping of the GW field is hence scale selective, so that small scales are damped more strongly. Generally it is found, by comparison against the LES data, that the static-stability criterion tends to generate turbulence too quickly. This might be explained by phase cancellations between different spectral components so that higher amplitudes are required to really lead to the onset of turbulence. Nonetheless the turbulence scheme works quite well if validated against the LES simulations.

Finally also a steady-state WKB model has been implemented, representing the approach in current GW-drag parameterizations. Caustics are not an issue in such a context so that a spectral formulation is not necessary. The simulations discussed here consider locally monochromatic GW fields that are damped to the saturation limit once static instability is diagnosed. Spectral extensions have been considered as well (not shown), but these did not yield substantially different results.

The pattern observed in our simulations is quite clear: whenever a wave-impact on the mean flow is observed, the direct GW-mean-flow interactions dominate over the wave-breaking effect. It is important that these interactions depend on wave transience. Without the latter they would not be possible - due to the non-acceleration paradigm - without onset of turbulence. Interesting effects arise that would be missed by a steady-state scheme. An example is partial reflection from a jet that would not occur within linear theory. The wave-induced wind contributes sufficiently so that part of the GW packet substantially changes its propagation. In the various turbulent cases considered, be it apparent wave breaking by direct static instability or triggered by modulational instability, we see a dominant impact from direct GW-mean-flow interactions as well. Even when the turbulence scheme is suppressed the results between transient WKB and LES agree to leading order, at least as far as the spatial distribution of wave energy and mean wind are concerned. Turbulence acts to next order and ensures the correct dissipation of total energy.

Turbulence without direct GW-mean-flow interactions, however fails to explain the LES data: the steady-state WKB simulations exhibit way too strong damping of the GW energy, and also the mean flow is underestimated significantly. This argues for a serious attempt at including GW-transience effects into GW-drag parameterizations. Undoubtedly the implementation of transient WKB into climate and weather models will face considerable efficiency issues. The strong role we see for direct GW-mean-flow interactions could provide motivation, however, to overcome these.

A final caveat might be in place that, notwithstanding the apparent success of transient WKB seen here, there are plenty of cases where this approach might also find its limitations. Not only have we neglected lateral GW propagation, an effect known to also be potentially important (Bühler and McIntyre 2003; Senf and Achatz 2011; Ribstein et al. 2015), but the limits of WKB as a whole will be reached where strong wave-wave interactions come into play, or where significant small-scale structures are present (Fritts et al. 2013).

Acknowledgments. U.A. and B.R. thank the German Federal Ministry of Education and Research (BMBF) for partial support through the program *Role of the Middle Atmosphere in Climate (ROMIC)* and through grant 01LG1220A. U.A. and J.W. thank the German Research Foundation (DFG) for partial support through the research unit *Multiscale Dynamics of Gravity Waves (MS-GWaves)* and through grants AC 71/8-1, AC 71/9-1, and AC 71/10-1.

References

Achatz, U., 2005: On the role of optimal perturbations in the instability of monochromatic gravity waves. *Phys. Fluids*, **17**, 094 107 1–27.

Achatz, U., 2007: Gravity-wave breaking: Linear and primary nonlinear dynamics. *Adv. Space Res.*, 719–733, doi:10.1016/j.asr.2007.03.078.

Achatz, U., R. Klein, and F. Senf, 2010: Gravity waves, scale asymptotics and the pseudo- incompressible equations. *J. Fluid Mech.*, **663**, 120–147, doi:10.1017/S0022112010003411.

Alexander, M. J., and T. J. Dunkerton, 1999: Gravity waves, scale asymptotics and the pseudo-incompressible equations. *J. Atmos. Sci.*, **56**, 4167–4182.

Alexander, M. J., and Coauthors, 2010: Review article, recent developments in gravity-wave effects in climate models and global distribution of gravity-wave momentum flux from observations and models. *Quart. J. Roy. Meteor. Soc.*, **136**, 1103–1124, doi:10.1002/qj.637.

Becker, E., 2004: Direct heating rates associated with gravity wave saturation. *J. Atmos. Sol.-Terr. Phys.*, **66**, 683–696.

Berethon, F. P., 1966: The propagation of groups of internal gravity waves in a shear flow. *Quart. J. Roy. Meteor. Soc.*, **92**, 466–480.

Broutman, D., J. W. Rottman, and S. D. Eckermann, 2004: Ray methods for internal waves in the atmosphere and ocean. *Annu. Rev. Fluid. Mech.*, **36**, 233–253.

Bühler, O., and M. E. McIntyre, 1999: On shear-generated gravity waves that reach the mesosphere. part ii: Wave propagation. *J. Atmos. Sci.*, **56**, 3764–3773.

Bühler, O., and M. E. McIntyre, 2003: Remote recoil: a new wave-mean interaction effect. *J. Fluid Mech.*, **492**, 207–230.

Bühler, O., and M. E. McIntyre, 2005: Wave capture and wave-vortex duality. *J. Fluid Mech.*, **534**, 67–95, doi:10.1017/S0022112005004374.

Butchart, N., 2014: The brewer-dobson circulation. *Rev. Geophys.*, **52**, 157–184, doi:10.1002/2013RG000448.

Dosser, H. V., and B. Sutherland, 2011: Anelastic internal wave packet evolution and stability. *J. Atmos. Sci.*, **68**, 2844–2859, doi:10.1175/JAS-D-11-097.1.

Dunkerton, T. J., 1997: The role of gravity waves in the quasi biennial oscillation. *J. Geophys. Res.*, **102**, 26 053–26 076.

Durran, D. R., 1989: Improving the anelastic approximation. *J. Geophys. Res.*, **46**, 1453–1461.

Eckermann, S. D., and P. Preusse, 1999: Global measurements of stratospheric mountain waves from space. *Science*, **286**, 1534–1537.

Fritts, D., and M. J. Alexander, 2003: Gravity wave dynamics and effects in the middle atmosphere. *Rev. Geophys.*, **41(1)**, 1003, doi:10.1029/2001RG000106,2003.

Fritts, D. C., C. Bizon, J. A. Werne, and C. K. Meyer, 2003: Layering accompanying turbulence generation due to shear instability and gravity-wave breaking. *J. Geophys. Res.*, **108**, 8452, doi:10.1029/2002JD002406.

Fritts, D. C., S. L. Vadas, K. Wan, and J. A. Werne, 2006: Mean and variable forcing of the middle atmosphere by gravity waves. *J. Atmos. Sol.-Terr. Phys.*, **68**, 247–265.

Fritts, D. C., L. Wang, J. Werne, T. Lund, and K. Wan, 2009: Gravity wave instability dynamics at high reynolds numbers, 1: Wave field evolution at large amplitudes and high frequencies. *J. Atmos. Sci.*, **66**, 1126–1148.

Fritts, D. C., L. Wang, and J. A. Werne, 2013: Gravity wave-fine structure interactions. part i: Influences of fine structure form and orientation on flow evolution and instability. *Journal of the*

Atmospheric Sciences, **70 (12)**, 3710–3734, doi:10.1175/JAS-D-13-055.1, URL http://dx.doi.org/10.1175/JAS-D-13-055.1, http://dx.doi.org/10.1175/JAS-D-13-055.1.

Grimshaw, R., 1975: Nonlinear internal gravity waves in a rotating fluid. *J. Fluid Mech.*, **71**, 497–512.

Hertzog, A., C. Souprayen, and A. Hauchecorne, 2002: Eikonal simulations for the formation and the maintenance of atmospheric gravity wave spectra. *J. Fluid Mech.*, **107**, 4145, doi:10.1029/2001JD000815.

Hickel, S., N. A. Adams, and J. Domaradzki, 2006: An adaptive local deconvolution model for implicit les. *J. Comput. Phys.*, **213**, 413–436, doi:10.1016/.j.jcp.2005.08.017.

Hines, C. O., 1997a: Doppler spread gravity-wave parametrization of momentum deposition in the middle atmosphere. part 1: Basic formulation. *J. Atmos. Sol. Terr. Phys.*, **59**, 371–386.

Hines, C. O., 1997b: Doppler spread gravity-wave parametrization of momentum deposition in the middle atmosphere. part 2: Broad spectra and quasi monochromatic spectra, and implementation. *J. Atmos. Sol. Terr. Phys.*, **59**, 387–400.

Holton, J. R., and R. S. Lindzen, 1972: An updated theory for the quasi-biennial cycle of the tropical stratosphere. *J. Atmos. Sci.*, **76**, 1076–1080.

Houghton, J. T., 1978: The stratosphere and mesosphere. *Quart. J. Roy. Meteor. Soc.*, **104**, 1–29, doi:10.1002/qj.49710443902.

J.Coiffier, 2011: *Numerical Weather Prediction*. 2nd ed., Cambridge University Press, 340 pp.

Kim, Y.-J., D. S. Eckermann, and H. Chund, 2003: An overview of past, present and future gravity-wave drag parametrization for numerical climate and weather prediction models. *Atmos.–Ocean*, **41**, 65–98, doi:10.3137/ao.410105.

Limpasuvana, V., J. H. Richter, Y. Orsolinic, F. Stordald, and O. Kvisseld, 2012: The roles of planetary and gravity waves during a major stratospheric sudden warming as characterized in waccm. *J. Atmos. Sol. Terr. Phys.*, **78–79**, 84–98, doi:10.1016/j.jastp.2011.03.004.

Lindzen, R. S., 1981: Turbulence and stress owing to gravity wave and tidal breakdown. *J. Geophys. Res.*, **86**, 9707–9714, doi:10.1029/JC086iC10p09707.

Lombard, P., and J. Riley, 1996: Instability and breakdown of internal gravity waves. I. Linear stability analysis. *Phys. Fluids*, **8**, 3271–3287.

Lott, F., and L. Guez, 2013: A stochastic parameterization of the gravity waves due to convection and its impact on the equatorial stratosphere. *J. Geophys. Res.*, **118**, 8897–8909, doi:10.1002/jgrd.50705,2013.

Lott, F., and M. Miller, 1997: A new subgrid-scale orographic drag parametrization: Its formulation and testing. *Quart. J. Roy. Meteor. Soc.*, **123**, 101–127.

Marks, C., and S. Eckermann, 1995: A three-dimensional nonhydrostatic ray-tracing model for gravity waves: Formulation and preliminary results for the middle atmosphere. *J. Atmos. Sci.*, **52**, 1959–1984.

Marks, C., and S. Eckermann, 1997: GROGRAT: A new model of the global propagation and dissipation of atmospheric gravity waves. *Adv. Space Res.*, **20**, 1253–1256.

Medvedev, A. S., and G. P. Klaassen, 1995: Vertical evolution of gravity wave spectra and the parametrization of associated gravity wave drag. *J. Geophys. Res.*, **100**, 25 841–25 854.

Muraschko, J., M. Fruman, U. Achatz, S. Hickel, and Y. Toledo, 2015: On the application of wentzel-kramer-brillouin theory for the simulation of the weakly nonlinear dynamics of gravity waves. *Quart. J. Roy. Meteor. Soc.*, **141**, 676–697, doi:10.1002/qj.2381.

Nappo, J. C., 2002: *An Introduction to Atmospheric Gravity Waves*. 1st ed., Academic Press, 276 pp.

Ribstein, B., U. Achatz, and F. Senf, 2015: The interaction between gravity waves and solar tides: Results from 4d ray tracing coupled to a linear tidal model. *J. Geophys. Res.*, **120**, 6795–6817, doi:10.1002/2015JA021349.

Richter, J. H., F. Sassi, and R. R. Garcia, 2010: Towards a physically based gravity wave source parameterization. *J. Atmos. Sci.*, **67**, 136–156, doi:10.1175/2009JAS3112.1.

Rieper, F., U. Achatz, and R. Klein, 2013a: Range of validity of an extended wkb theory for atmospheric gravity waves: one dimensional and two dimensional case equations with implicit turbulence parameterization. *J. Fluid Mech.*, **729**, 330–363, doi:10.1017/jfm.2013.307.

Rieper, F., S. Hickel, and U. Achatz, 2013b: A conservative integration of the pseudo-incompressible equations with implicit turbulence parameterization. *Mon. Wea. Rev.*, **141**, 861–886, doi:10.1175/MWR-D-12-00026.1.

Scaife, A. A., J. R. Knight, G. K. Vallis, and C. K. Folland, 2005: A stratospheric influence on the winter nao and north atlantic surface climate. *Geophys. Res. Let.*, **32**, (18) L18 715,, doi: 10.1029/2005GL023226.

Scaife, A. A., and Coauthors, 2012: Climate change projections and stratosphere-troposphere interaction. *Clim. Dyn.*, **38**, 2089–2097, doi:10.1007/s00382-011-1080-7.

Senf, F., and U. Achatz, 2011: On the impact of middle-atmosphere thermal tides on the propagation and dissipation of gravity waves. *J. Geophys. Res.*, **116**, D24 110, doi:10.1029/2011JD015794.

Sutherland, B. R., 2006: Weakly nonlinear internal gravity wavepackets. *J. Fluid Mech.*, **569**, 249–258, doi:10.1017/S0022112006003016.

Sutherland, B. R., 2010: Internal gravity waves. *Cambridge University Press*, 377.

van Leer, B., 1979: Towards the ultimate conservative difference scheme, v. a second order sequel to godunov's method. *J. Comp. Phys.*, **32**, 101–136.

Warner, C. D., and M. E. McIntyre, 2001: An ultrasimple spectral parametrization for nonorographyic gravity waves. *J. Atmos. Sci.*, **58**, 1837–1857.

LIST OF TABLES

TABLE 1. Settings used in the idealised cases (part 1)

Experiment	**Wavepacket**	**Background**	**Domain size**	**Resolution**
REFR Refraction by a jet	Cosine shape $\lambda_x = 10km$, $\lambda_z = 1km$ $k = 2\pi/\lambda_x, m = 2\pi/\lambda_z$ $z_0 = 10km, \Delta_{wp} = 10km$ $branch = -1, a_0 = 0.1$	non-Boussinesq $T = 300K$ $N \approx 0.018$ $u_0 = 5m/s$ $z_u = 25km$ $\Delta_u = 10km$	WKB Euler: $L_z = 40km$ $m \in [0.001, 0.008]$ WKB Lagrange: $L_z = 40km$ LES: $L_z = 40km, L_x = 10km$	WKB Euler: $nz = 400, nm = 70$ $dz \approx 100m, dm = 10^{-4}s^{-1}$ WKB Lagrange: $nz = 400, dz_{smooth} \approx 600m$ $dz \approx 100m, n_{ray} = 4000$ LES: $nz = 1280, nx = 32$ $dz \approx 31m, dx = 310m$
REFL Reflection from a jet	Cosine shape $\lambda_x = 10km$, $\lambda_z = 1km$ $k = 2\pi/\lambda_x, m = 2\pi/\lambda_z$ $z_0 = 10km, \Delta_{wp} = 10km$ $branch = -1, a_0 = 0.1$	non-Boussinesq $T = 300K$ $N \approx 0.018$ $u_0 = 40m/s$ $z_u = 25km$ $\Delta_u = 10km$	WKB Euler: $L_z = 40km$ $m \in [-0.01, 0.008]$ WKB Lagrange: $L_z = 40km$ LES: $L_z = 40km, L_x = 10km$	WKB Euler: $nz = 400, nm = 180$ $dz \approx 100m, dm = 10^{-4}s^{-1}$ WKB Lagrange: $nz = 400, dz_{smooth} \approx 600m$ $dz \approx 100m, n_{ray} = 4000$ LES: $nz = 2500, nx = 64$ $dz \approx 16m, dx = 156m$
PREFL Partial Reflection from a jet	Cosine shape $\lambda_x = 6km$, $\lambda_z = 3km$ $k = 2\pi/\lambda_x, m = 2\pi/\lambda_z$ $z_0 = 10km, \Delta_{wp} = 10km$ $branch = -1, a_0 = 0.1$	non-Boussinesq $T = 300K$ $N \approx 0.018$ $u_0 = 9,75m/s$ $z_u = 25km$ $\Delta_u = 10km$	WKB Lagrange: $L_z = 50km$ LES: $L_z = 50km, L_x = 6km$	WKB Lagrange: $nz = 166, dz_{smooth} \approx 1800m$ $dz \approx 300m, n_{ray} = 4320$ LES: $nz = 538, nx = 32$ $dz \approx 93m, dx = 187m$

TABLE 2. Settings used in the idealised cases (part 2)

STIH Static Instability Hydrostatic Wavepacket	Gaussian shape $\lambda_x = 30km$, $\lambda_z = 3km$ $k = 2\pi/\lambda_x, m = 2\pi/\lambda_z$ $z_0 = 10km, \Delta_{wp} = 25km$ $branch = -1, a_0 = 0.5$	non-Boussinesq $T = 300K$ $N \approx 0.018$	WKB Lagrange: $L_z = 80km$ LES: $L_z = 80km, L_x = 30km$	WKB Lagrange: $nz = 266, dz_{smooth} \approx 1800m$ $dz \approx 300m, n_{ray} = 4320$ LES: $nz = 854, nx = 32$ $dz \approx 94m, dx \approx 940m$
STINH Static Instability Non-hydrostatic Wavepacket	Gaussian shape $\lambda_x = 1km$, $\lambda_z = 1km$ $k = 2\pi/\lambda_x, m = 2\pi/\lambda_z$ $z_0 = 10km, \Delta_{wp} = 10km$ $branch = -1, a_0 = 0.9$	non-Boussinesq $T = 300K$ $N \approx 0.018$	WKB Lagrange: $L_z = 30km$ LES: $L_z = 30km$, $L_x = 1km$	WKB Lagrange: $nz = 300, dz_{smooth} \approx 600m$ $dz \approx 100m, n_{ray} = 4000$ LES: $nz = 960, nx = 32$ $dz \approx 31m, dx \approx 310m$
MI Modulational Instability	Cosine shape $\lambda_x = 1km$, $\lambda_z = 1km$ $k = 2\pi/\lambda_x, m = 2\pi/\lambda_z$ $z_0 = 10km, \Delta_{wp} = 20km$ $branch = -1, a_0 = 0.1$	non-Boussinesq $T = 300K$ $N \approx 0.018$	WKB Lagrange: $L_z = 60km$ LES: $L_z = 60km$, $L_x = 1km$	WKB Lagrange: $nz = 600, dz_{smooth} \approx 600m$ $dz \approx 100m, n_{ray} = 4000$ LES: $nz = 1920, nx = 32$ $dz \approx 31m, dx \approx 310m$
CL Critical Layer	Cosine shape $\lambda_x = 10km$, $\lambda_z = 1km$ $k = 2\pi/\lambda_x, m = 2\pi/\lambda_z$ $z_0 = 10km, \Delta_{wp} = 10km$ $branch = -1, a_0 = 0.1$	non-Boussinesq $T = 300K$ $N \approx 0.018$ $u_0 = -11m/s$ $z_u = 25km$ $\Delta_u = 10km$	WKB Lagrange: $L_z = 30km$ LES: $L_z = 30km$, $L_x = 10km$	WKB Lagrange: $nz = 300, dz_{smooth} \approx 600m$ $dz \approx 100, n_{ray} = 4000$ LES: $nz = 960, nx = 32$ $dz \approx 31m, dx \approx 310m$

LIST OF FIGURES

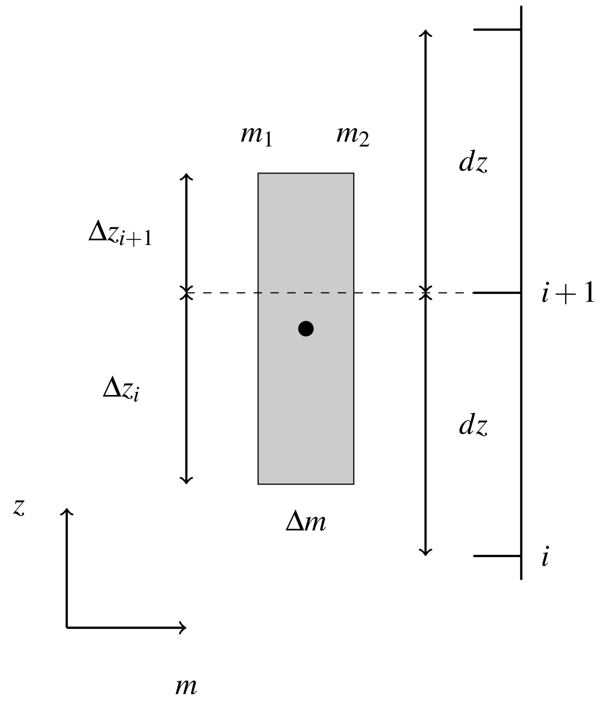

FIG. 1. Schematic illustration of a ray volume in the Lagrangian transient WKB simulation.

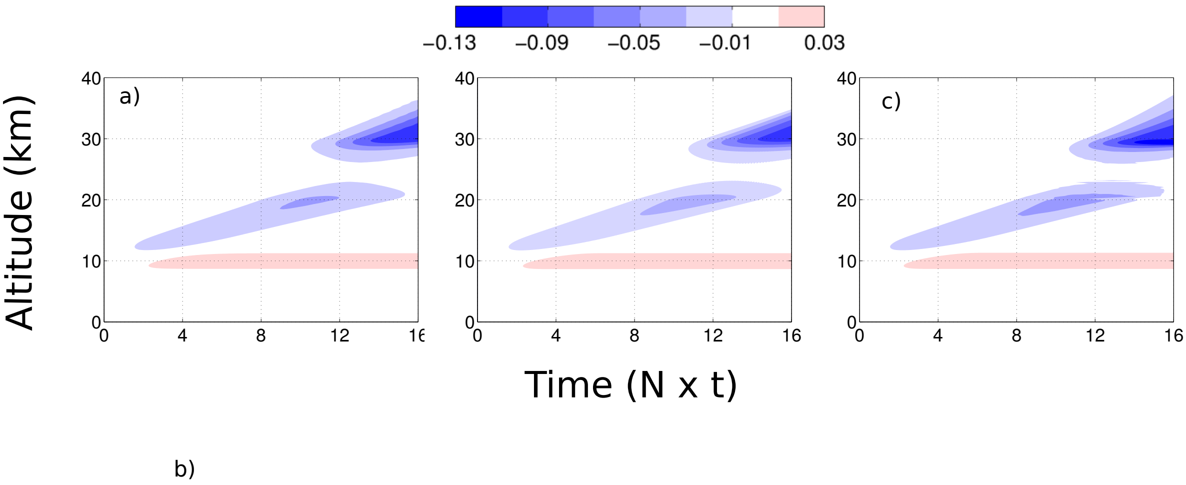

FIG. 2. Shaded contours: Hovmöller diagram of the wave induced wind (ms^{-1}) for the case **REFR** where a hydrostatic GW packet ($\lambda_x = 10km, \lambda_z = 1km$) is refracted by a weak jet ($u_0 = 5ms^{-1}$); (a) LES, (b) Lagrangian transient WKB simulation, (c) Eulerian transient WKB simulation.

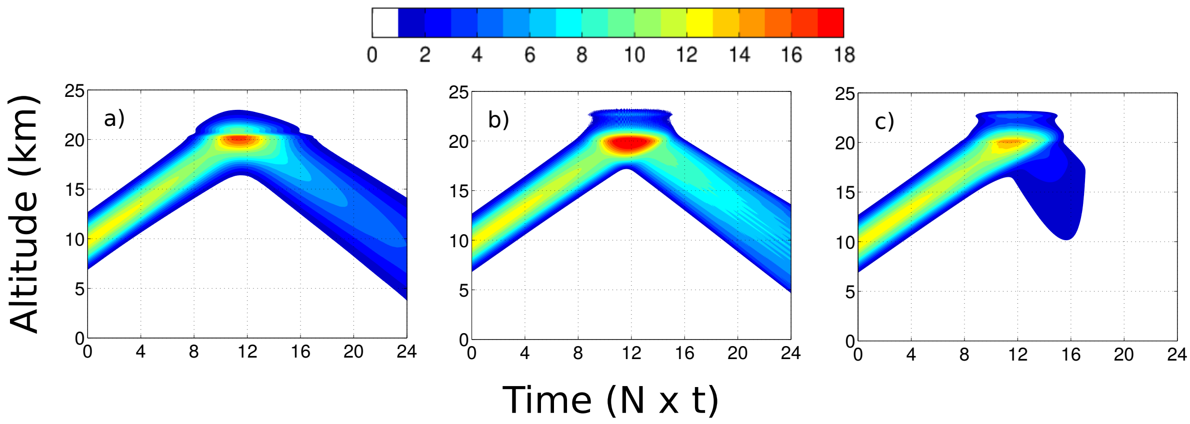

FIG. 3. Hovmöller diagram of the wave energy (m^2s^{-2}) for the case **REFL** where a hydrostatic GW packet ($\lambda_x = 10km, \lambda_z = 1km$) is reflected from a strong jet ($u_0 = 40ms^{-1}$); (a) LES, (b) Lagrangian transient WKB simulation, (c) Eulerian transient WKB simulation.

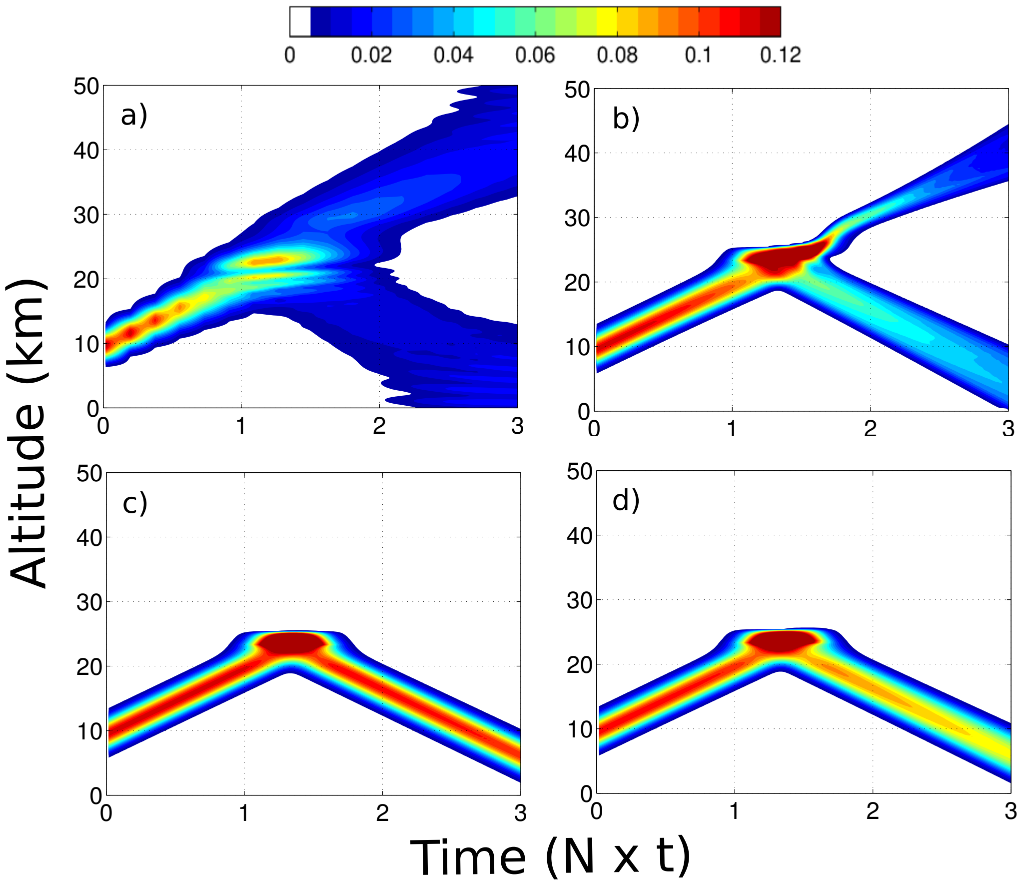

757 FIG. 4. Hovmöller diagram of the wave energy (m^2s^{-2}) for the case **PREFL** where a weakly hydrostatic GW packet ($\lambda_x = 6km, \lambda_z = 3km$) is partly refracted by and partly reflected from a jet ($u_0 = 9.75ms^{-1}$); (a) LES, (b) Lagrangian transient WKB simulation, (c) Lagrangian WKB model with decoupled GW and mean flow, (d) Lagrangian transient WKB simulation with a Boussinesq reference medium.

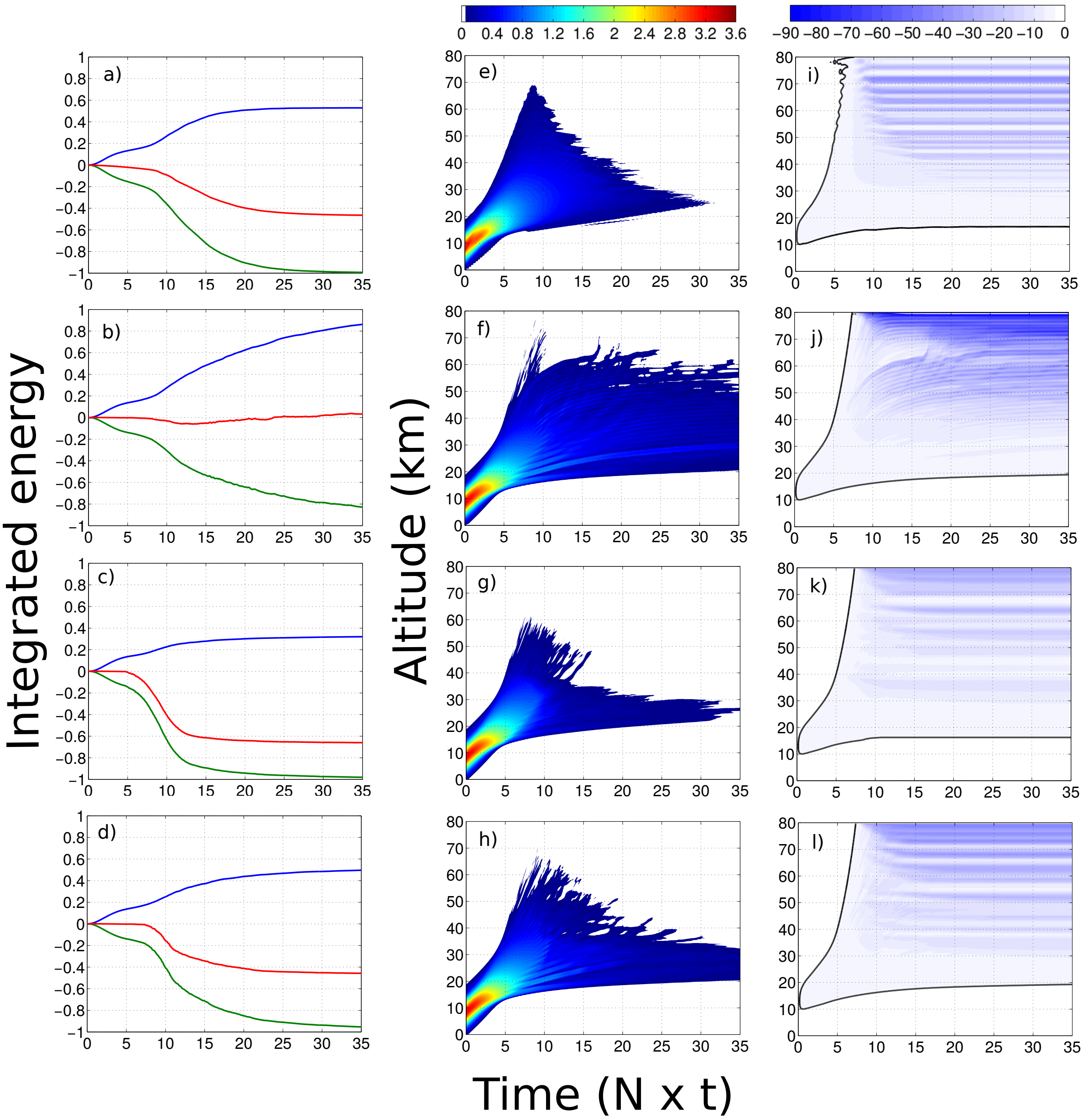

FIG. 5. Time evolution of normalized vertically integrated energy (non-dimensional) of the GW packet (green), the mean flow (blue) and their sum (red) (a)-(d); Hovmöller diagrams of the wave energy (m^2s^{-2}) (e)-(h) and the induced mean wind (ms^{-1}) (i)-(l); LES: (a),(e),(i), Lagrangian transient WKB simulation: (b),(f),(j), Lagrangian WKB model with saturation parametrization $\alpha = 1$: (c),(g),(k), Lagrangian transient WKB simulation with saturation parametrization $\alpha = 2$: (d),(h),(l) ; case **STIH** where a hydrostatic GW packet ($\lambda_x = 30km, \lambda_z = 3km$) is reaching static-instability during propagation. The solid black contours (value: -0.11) in panels (i)-(l) are added to help the visual comparison.

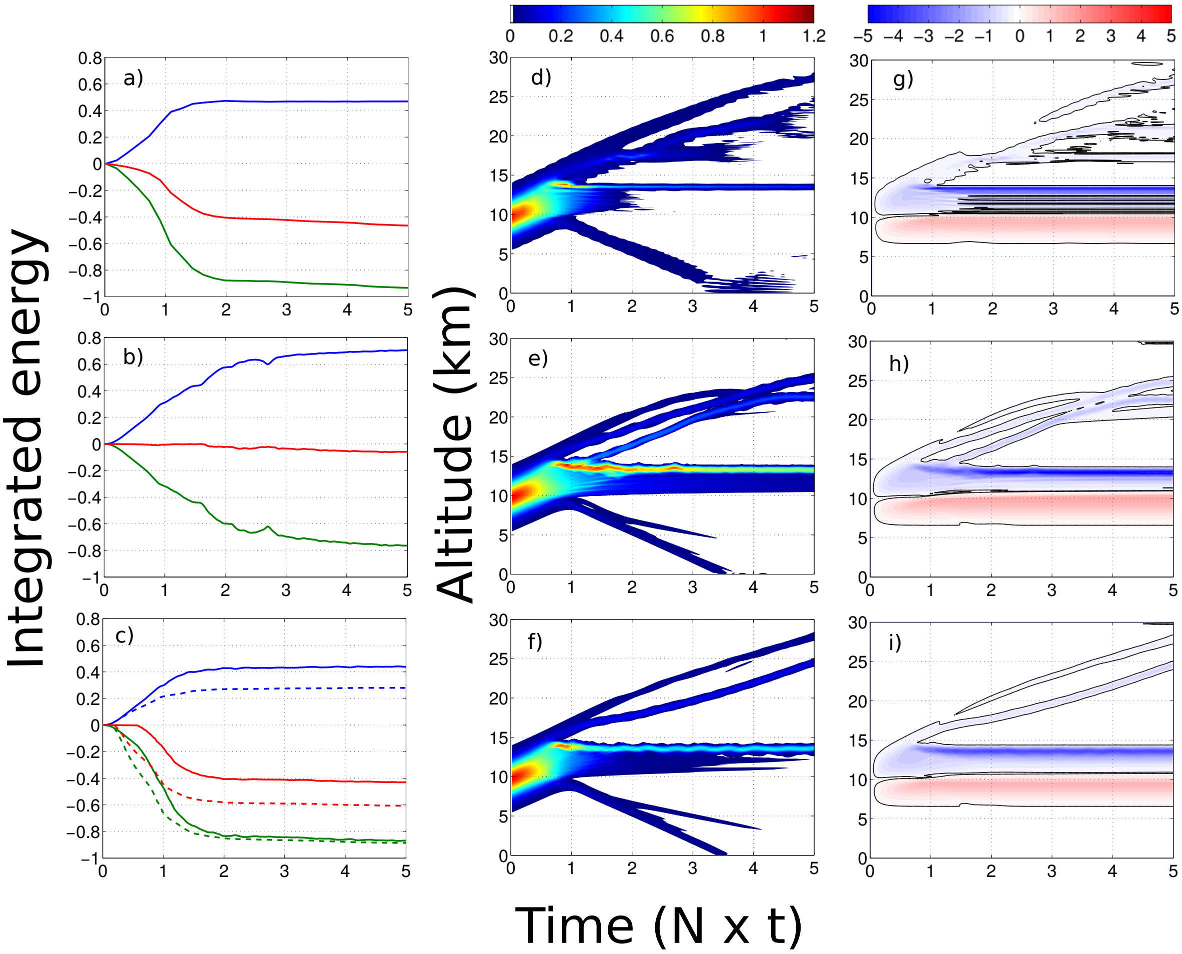

FIG. 6. Time evolution of normalized vertically integrated energy (non-dimensional) of the GW packet (green), the mean flow (blue) and their sum (red) (a)-(c); Hovmöller diagrams of the wave energy (m^2s^{-2}) (d)-(f) and the induced mean wind (ms^{-1}) (g)-(i); LES: (a),(d),(g), Lagrangian transient WKB simulation: (b),(e),(h), Lagrangian transient WKB simulation with saturation parametrization $\alpha = 1.4$: (c),(f),(i); dashed lines on panel (c) correspond to the Lagrangian transient WKB simulation with saturation parametrization $\alpha = 1$; case **STINH** where a non-hydrostatic GW packet ($\lambda_x = 1km, \lambda_z = 1km$) is reaching static-instability during propagation. The solid black contours (values: -0.1, 0.1) in panels (g)-(i) are added to help the visual comparison.

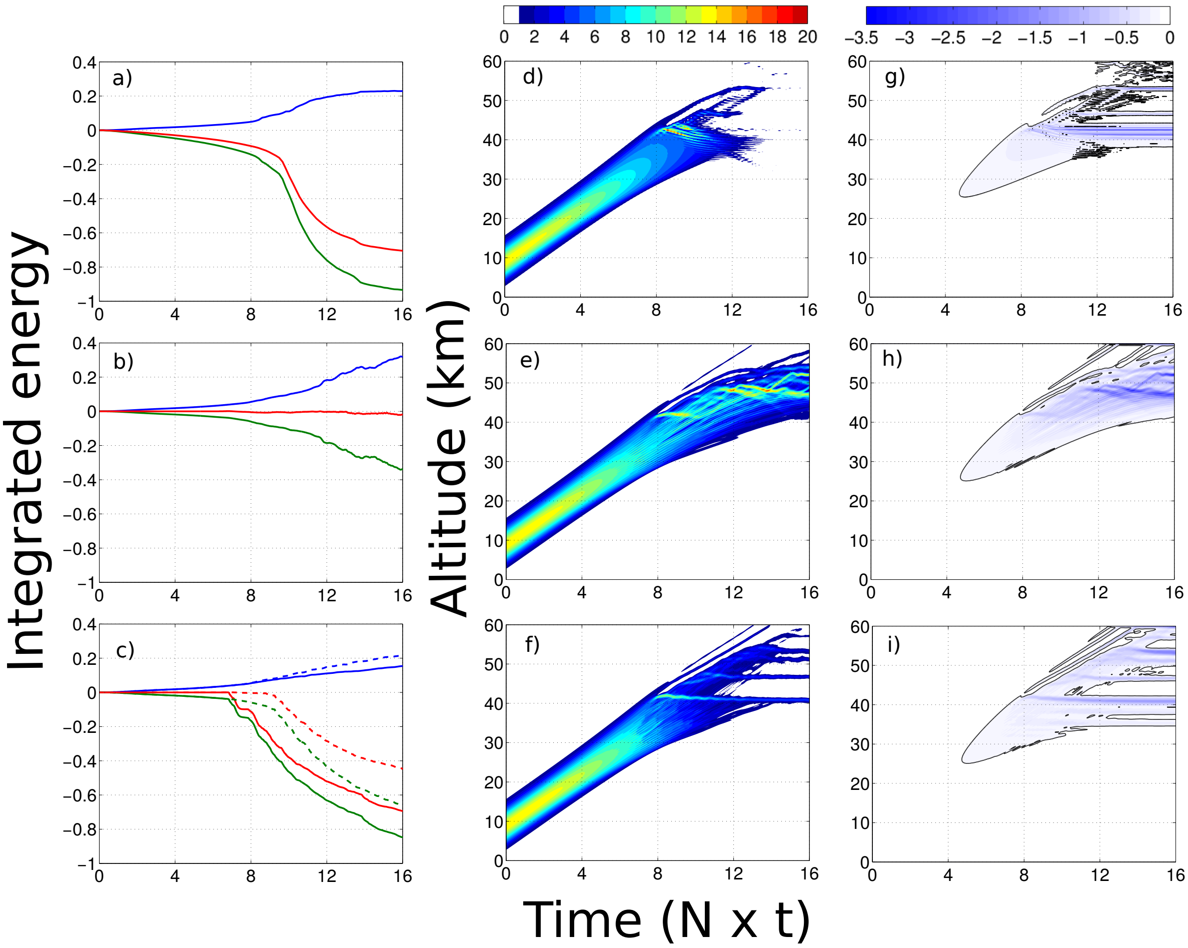

FIG. 7. The same as Fig.6 but with $\alpha = 0.6$ for the row (c),(f),(i); dashed lines on panel (c) correspond to the Lagrangian transient WKB simulation with saturation parametrization $\alpha = 1$; case **MI** where a non-hydrostatic GW packet ($\lambda_x = 1km, \lambda_z = 1km$) is becoming modulationally unstable during propagation. The solid black contours (value: -0.1) in panels (g)-(i) are added to help the visual comparison.

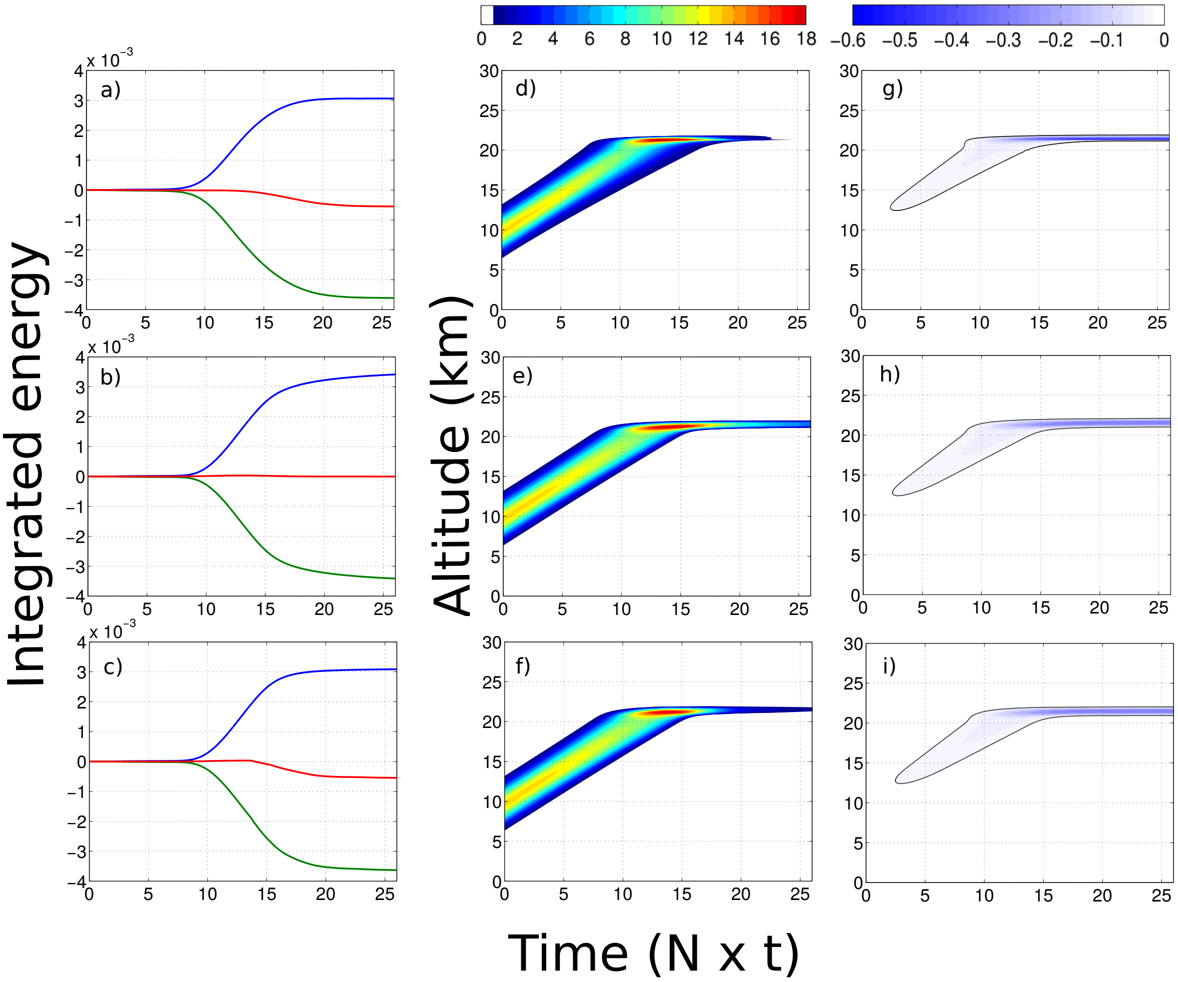

FIG. 8. Time evolution of normalized vertically integrated energy (non-dimensional) of the GW packet (green), the mean flow (blue) and their sum (red) (a)-(c); Hovmöller diagram of the wave energy (m^2s^{-2}) (d)-(f) and the induced mean wind (ms^{-1}) (g)-(i); LES: (a),(d),(g), Lagrangian WKB model: (b),(e),(h), Lagrangian transient WKB simulation with saturation parametrization $\alpha = 1$: (c),(f),(i); case **CL** where a hydrostatic GW packet ($\lambda_x = 10km, \lambda_z = 1km$) is reaching a critical layer due to a jet ($u_0 = -11ms^{-1}$). The solid black contours (value: -0.015) in panels (g)-(i) are added to help the visual comparison.

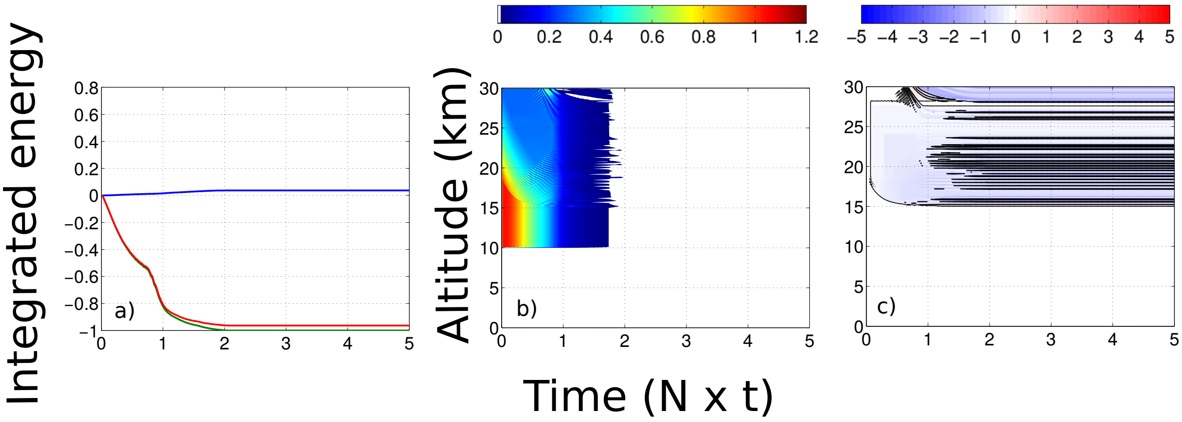

FIG. 9. Same as Fig. 6 but obtained with the steady-state WKB model.